FFI-RAPPORT

17/17096

Reducing vibrations caused by the radome at P-3C Orion: A numerical simulation study

–

Carl Erik Wasberg
Øyvind Andreassen
Anders Helgeland

Reducing vibrations caused by the radome at P-3C Orion: A numerical simulation study

Carl Erik Wasberg
Øyvind Andreassen
Anders Helgeland

Norwegian Defence Research Establishment (FFI) 24 January 2018

Keywords

Fly
Vibrasjoner
Radomer
Aerodynamikk
Computational Fluid Dynamics (CFD)

FFI-RAPPORT:
2017/17096

Project number:
5262

ISBN:
P: 978-82-464-3016-4
E: 978-82-464-3017-1

Approved by:
Janet Martha Blatny, *Director*
Anders Helgeland, *Research Manager*

Summary

Around 1999, a new instrument was mounted on the underbelly of the P-3C aircrafts. The enclosure proctecting the instrument is called a *radome*. The radome has caused increased levels of vibrations in the aircrafts, strongest in the aft part. It was believed that the origin of the vibrations came from the radome itself, due to fluid-structure interactions at the radome. Later, vibration measurements and Computational Fluid Dynamics (CFD) simulations have revealed that the vibrations are caused by interactions of the turbulent wake, generated by the radome, and the fuselage.

It has been shown previously that the shape of the radome is the cause of massive flow separation, resulting in a strongly turbulent wake. Previous CFD simulations have shown that including a fairing system attached to the radome, called “Wedge” in this report, causes a reduction in the area of separation and reduces the strength of the vortices and flow fluctuations. The consequence would be reduced strength of the flow-hull interactions and vibration level. This was confirmed by a series of test flights performed in 2012, where the use of the “Wedge” was found to reduce the energy of the vibrations by around 50 percent.

Hatches and equipment attached to the aircraft imposed strong restrictions on the size of the fairing. The line of sight of the instrument should not be influenced, ruling out changes to the spherical part of the radome. Even with such restrictions in fairing design, a good reduction of the vibration level was achieved.

The question addressed in this work is what could be achieved with fewer restrictions, and this led to a new, more streamlined, radome shape called “Droplet”. CFD simulations containing the “Droplet” show improved results compared with the “Wedge”. The areas of flow separation become smaller and the strength of the wake vortices is much weaker compared with all other simulation cases considered.

In addition to CFD analysis on the “Droplet” and “Wedge” configurations, we have included CFD analysis on an alternative design, consisting of a splitter plate behind the radome. This design was presented in a report on water tunnel tests by *L3 Communications* in 2010 as one of the configurations that were predicted to reduce the vibrations sufficiently. The main feature of the “Splitter plate” is to suppress the alternating vortex shedding from the radome, thus leading to a more symmetric behaviour of the flow. However, the simulations presented here reveal that the extension of the wake and the strength of the vortices are nearly equal to that of the original radome. We therefore believe that there exist better vibration reducing measures than the “Splitter plate”.

The analysis presented in this report shows that the “Droplet” is by far the best of the three vibration reducing measures “Droplet”, “Wedge”, and “Splitter plate”.

Sammendrag

Rundt 1999 ble det montert et nytt måleinstrument under P-3C-flyene. Instrumentet er bygget inn i en beskyttende struktur, kalt en *radom*. Radomen har medført økte vibrasjonsnivåer i flyene, sterkest i den bakre delen. En tidlig hypotese var at vibrasjonene hadde sin opprinnelse i selve radomen, gjennom fluid-struktur-interaksjoner på radomen. Senere har målinger og aerodynamikk-simuleringer avdekket at vibrasjonene skyldes vekselvirkningen mellom det turbulente kjølvannet, generert av radomen, og flykroppen.

Det er tidligere vist at formen på radomen forårsaker massiv separasjon av strømningen. Dette fører til et sterkt turbulent kjølvann bak radomen. Tidligere CFD (Computational Fluid Dynamics)-simuleringer har vist at ved å sette en såkalt "fairing" på radomen, i form av en kileaktig utvidelse på baksiden, oppnås mindre separasjonsområde i strømningen og redusert virvelstyrke og strømningsfluktuasjoner. Dette ville gi svakere vekselvirkninger mellom strømningen og skroget, og følgelig redusert vibrasjonsnivå. Dette ble bekreftet ved testflyvninger i 2012, der bruken av denne "Wedge" (kile)-modifikasjonen reduserte vibrasjonsenergien med rundt 50 prosent.

Luker og utstyr montert på flyet la sterke begrensninger på størrelsen på eventuelle fairinger. Synslinjen fra instrumentet skulle ikke påvirkes, noe som utelukket muligheten til å dekke til den sfæriske enden av radomen. Selv med slike begrensninger ble det oppnådd gode resultater med "Wedge"-modifikasjonen.

Spørsmålet som er stilt i dette arbeidet er hva som kan oppnås med færre designrestriksjoner, og dette har ført til en mer strømlinjeformet radom som vi kaller "Droplet" (dråpe). Simuleringer med denne formen gir enda bedre resultater enn det som ble oppnådd med "Wedge". Områdene hvor strømningen separerer, er mindre, og kjølvannsvirvlene blir mye svakere enn for alle andre fairing-geometrier som er simulert.

I tillegg til "Droplet"- og "Wedge"-konfigurasjonene er det gjort CFD-analyse av et alternativt design, som består av en splitter-plate bak radomen. Dette designet ble presentert i en rapport om vanntunnel-eksperimenter fra *L3 Communications* i 2010 som en av konfigurasjonene som skulle kunne dempe vibrasjonene tilstrekkelig mye. Hovedeffekten til denne "Splitter plate"-konfigurasjonen er å undertrykke den alternerende virvelavløsningen fra radomen og dermed gi et mer symmetrisk strømningsmønster. Simuleringene som er presentert her, viser imidlertid at bredden av kjølvannet og virvelstyrken er nesten de samme som for den originale radomen. Vi mener derfor at det finnes bedre løsninger for å redusere vibrasjoner enn en slik "Splitter plate".

Analysen i denne rapporten viser at "Droplet"-løsningen er den klart beste av de tre vibrasjonsdempende tiltakene "Droplet", "Wedge" og "Splitter plate".

Contents

1 Introduction

The radome (AS-105DF) mounted on the P-3C aircrafts is a source of vibrations that contribute to fatigue of structural components and are also unpleasant to the crew. A series of vibration measurements were performed by Lundberg in 2000 [1] and by Lundberg and Skaugen in 2002 [2] and 2004 [3, 4].

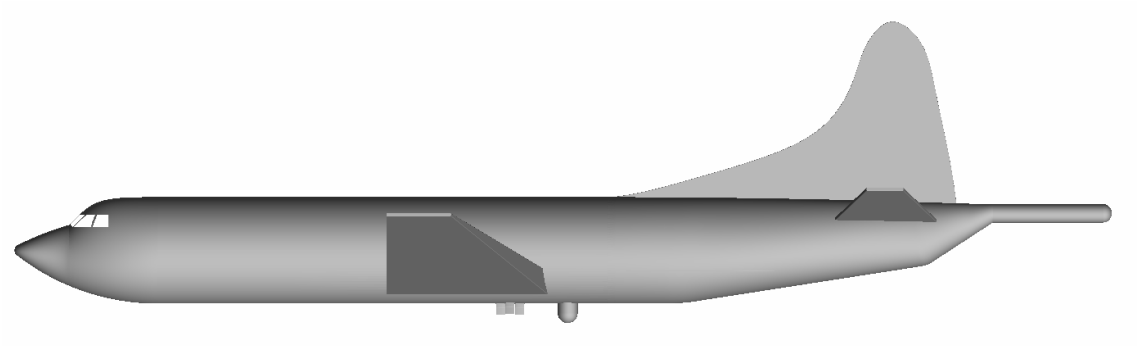

Figure 1.1 *A simplified model of the P-3C.*

A simplified model of the P-3C aircraft is shown in Figure 1.1, with the radome mounted on the underbelly, behind the wings. Numerical simulations of the flow field around the radome at P-3C Orion have been performed at FFI in 2003 [5, 6], 2004 [7] and 2012 [8]. Both the original radome design and different suggested modified geometries, designed to reduce the flow-induced vibrations on the aeroplane, have been considered.

Based on the simulation results in "Numerical simulations of flow-induced vibrations on Orion P-3C – extended study" [7], a first modification was built and tested in 2004, and the vibration results were reported in "Vibrasjonsmålinger på Orion P-3C 3298 med modifisert radardome – september 2004" [4]. The modification was small, due to very strict geometry limitations and practical considerations, and the measured results showed only minor improvements, and only at higher speeds.

New modifications of the radome shape, with more geometrical flexibility, were designed and simulated by FFI in 2012, and one of them was built and mounted on an aircraft. Simulation results and vibration measurements on the aircraft during the flight tests were reported in "Studies of aerodynamically induced vibrations on the P-3C maritime surveillance aircraft and proposed vibration reducing measures" [8]. The measurements showed that accelerations were all over reduced by 50% compared with the original radome configuration.

One of the requirements for the 2012 modifications was that the line of sight of the instrument should not be affected. The motivation for the present study is to explore the possibility for further improvement of the radome aerodynamics. It was also desired to increase the domain included in the simulations behind the radome, to include the effect of the fuselage curvature towards the tail of the aircraft.

This report is structured as follows: A review of the dominant fluid flow effects is given in Section 2, and the setup of the numerical simulations is described in Section 3, including a discussion of the

applied simplifications. The different geometrical configurations are presented in Section 4, and Section 5 contains a short description of the quantities that are extracted from the simulation for analysis and visualization purposes.

The simulation results are presented in Section 6, where RMS (Root Mean Square) values of force fluctuations are given in the first subsection, to present an overview. The next subsection contains pressure force results in the time- and frequency domains for the different configurations, and flow visualizations are presented in the final subsection. These visualizations are part of animations that are made to further illustrate the flow fields.

Section 7 contains the conclusions and some possible extensions, and, finally, some technical details about the numerical simulations are included in Appendix A.

2 Flow features

The original radome design can be described as a wall-mounted rounded cylinder, and there are three main mechanisms involved in the flow field.

Firstly, there is the alternating *vortex shedding* ("*von Kármán vortex street*") that occurs for flow past a cylinder. Secondly, a *horseshoe vortex*, generated by the flow stagnation at the front base of the cylinder (thereby also called "stagnation point vortex" or "leading edge vortex"), will wrap around the cylinder and have continued influence a long way downstream. And thirdly, the rounded end gives rise to separation at varying positions on the downstream part of the half-sphere, with resulting vortices that may move in seemingly random patterns in time. The full flow field is the result of the interaction between these three mechanisms.

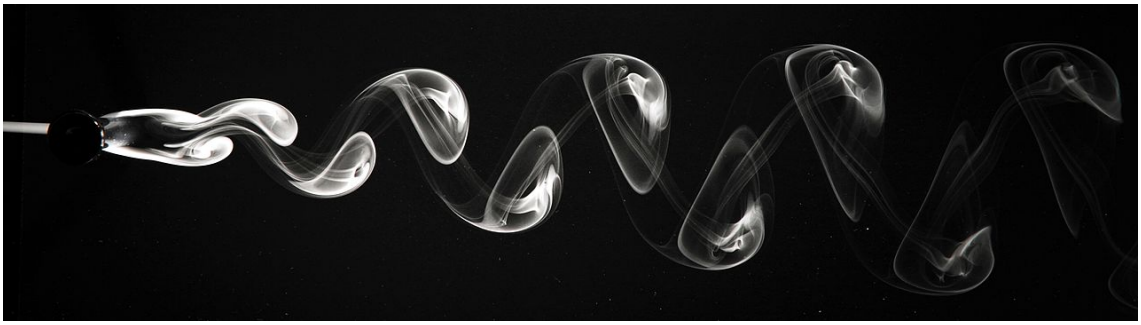

Figure 2.1 *Oil vapour visualization of the vortex street formed by air flow past a cylinder. (The black cylinder at the left, flow from left to right in the figure). Source: Wikimedia Commons, Jürgen Wagner*

A picture of a vortex street behind a cylinder is shown in Figure 2.1. Vortices are shedding from alternating sides, and the disturbances continue a long way downstream. This type of flow feature occurs for the part of a cylinder where end-effects can be ignored. For the radome, however, the flow field is strongly influenced by both the mounted end and the free rounded end, due to the relatively short cylindrical part. Consequently, the total picture becomes much more complex for the radome than for an idealized long cylinder.

Figure 2.2 shows a comparison between experimental ("Eksperiment") and Computational Fluid Dynamics ("CFD") results, reported in "Numerical simulations of flow-induced vibrations on Orion P-3C – extended study" [7]. The experiment was performed in a wind tunnel at the Turbulence Research Laboratory at Chalmers University of Technology (Gothenburg, Sweden), and friction-sensitive paint on one side of the model shows the flow pattern close to the surface. From the simulation, *wall friction lines* are drawn to produce the same effect. The vortex street interacts with the horseshoe vortex, causing it to oscillate sideways downstream.

All the three mentioned effects can be seen in the simulation picture of wall friction lines in Figure 2.3, taken from "Numerical simulations of flow-induced vibrations on Orion P-3C" [5]. In addition to the the horseshoe vortex and the shedded wake vortices, we see wall friction lines that end on the radome sphere, meaning that the flow separates from the surface and a vortex is formed.

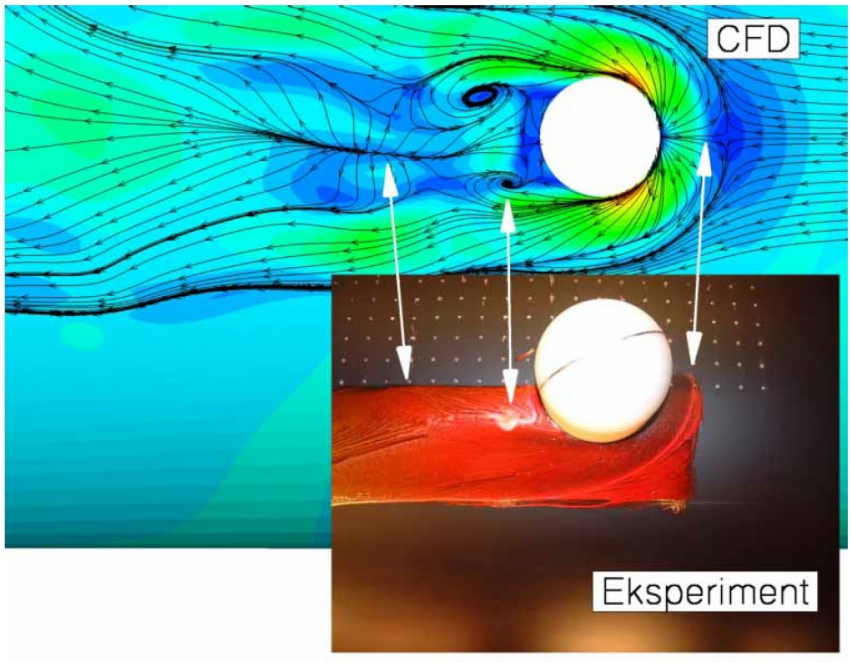

Figure 2.2 *Experimental and computational results of instantaneous wall friction lines in the vicinity of the radome, showing the horseshoe vortex and vortex shedding (from [7]). Flow from right to left in the figure.*

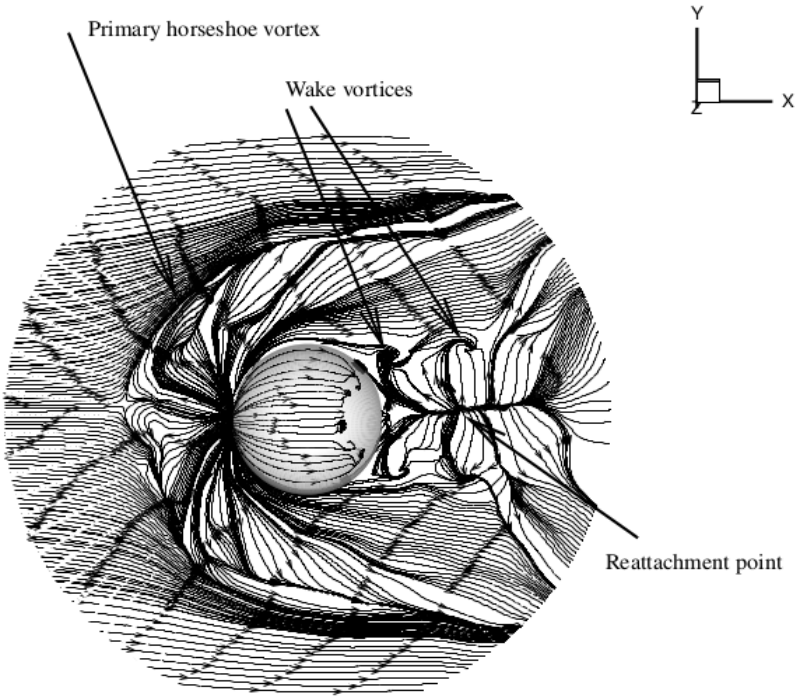

Figure 2.3 *Instantaneous wall friction lines (from [5]), showing the main flow features around the original radome. Flow from left to right in the figure.*

On a smooth half-sphere, there are no preferred positions for these separations, and the result is several chaotically moving vortices that interacts with the wake vortices to further increase the disturbances.

As discussed in the FFI reports by Reif and Wasberg from 2003 and 2004 mentioned above [5, 7], the main mechanism for the flow fluctuations is the coupling between the horseshoe vortex and the different vortices generated behind the radome. These effects are further illustrated and commented on in Section 6.3.

3 Simulation setup

The primary objective of the simulations is to model the flow field in the vicinity of the radome in sufficient detail to reproduce the unsteady shedding responsible for the observed low frequency vibrations.

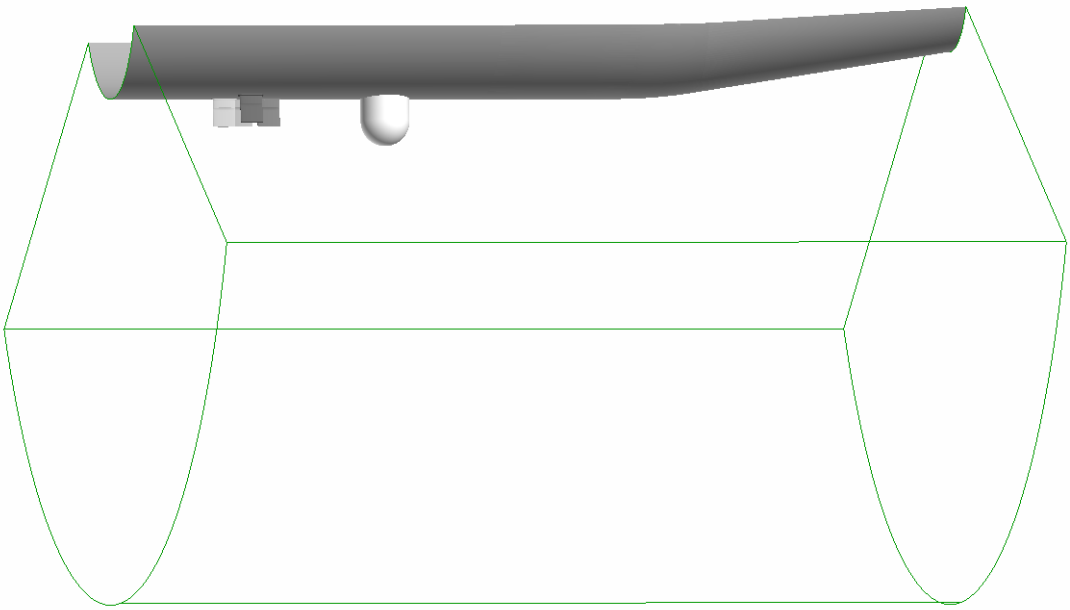

Figure 3.1 *The part of the aircraft body and the computational domain used in the numerical simulations.*

A numerical simulation of the flow around the full aircraft is not feasible with the desired level of detail and the available computational resources. The problem is therefore restricted to simulating the flow around the aircraft body near the radome. Apart from the four ACSL and Dual Band antennas situated 1–2 m in front of the radome, no geometrical details are included in the model. The computational domain used in the simulations, extending 6.72 m out from the fuselage and with a total length of 11.4 m, is shown in Figure 3.1.

This simplified configuration does not take into account two major effects on the aircraft. Firstly, the downwash effect from the wings, and secondly the propeller slip-stream. These effects greatly modifies the flow field aft the radome. However, the fundamental mechanisms responsible for the unsteady forcing are associated with the local wake dynamics downstream the radome rather than with the external flow field.

The list of simplifications can by summarized as follows:

Only a part of the aircraft is included:
The 2012 study [8] showed that the effects predicted by simulations were confirmed by measuring accelerations at different positions on the aircraft. This gives confidence in the simulation setup, which mainly provides relative differences between different configurations.

The background (far-field) flow field is constant, not including wing and propeller effects:
For the study of local flow phenomena around the radome, details of the background flow is not important, with the possible exception of a transverse component, as discussed later in this report.

The background (far-field) flow field is laminar:
Small-scale turbulence is in any case not calculated when a RANS (Reynolds-Averaged Navier-Stokes) turbulence model is used in the simulations. In the simulations, the boundary layer is formed in the area in front of the radome, and the presence of the antennas contribute to establish the turbulent boundary layer.

The fuselage geometry is simplified (only including antennas and the radome):
Small features would influence the boundary layer, but not the larger-scale features studied here.

All simulations are for zero angle of attack and sideslip:
Non-zero angles could be used, but the effect on oscillations would be small.

The present configuration is in our opinion sufficient to investigate the shedding and its associated *forcing* on a part of the aft fuselage.

The simulations are performed using the flow solver program Fluent from ANSYS Inc., solving the equations for incompressible, viscous fluid flow. The small-scale turbulent features are modelled using the unsteady Spalart-Allmaras RANS model [9]. More details about the numerical setup are given in Appendix A.

To predict the *response* of the aircraft would be a problem of a completely different magnitude, as the flow around the entire aircraft would have to be simulated, and coupled with a full structural model to calculate vibrations.

To predict whether vortices hit the vertical stabilizers and the boom of the aircraft requires simulations of a much larger scale. Again, the full flow field around the aircraft would be required to obtain a realistic model of the propagation of vortices away from the local area around the radome. The propeller slip-stream could presumably be modelled, and not computed in detail.

4 Simulation cases

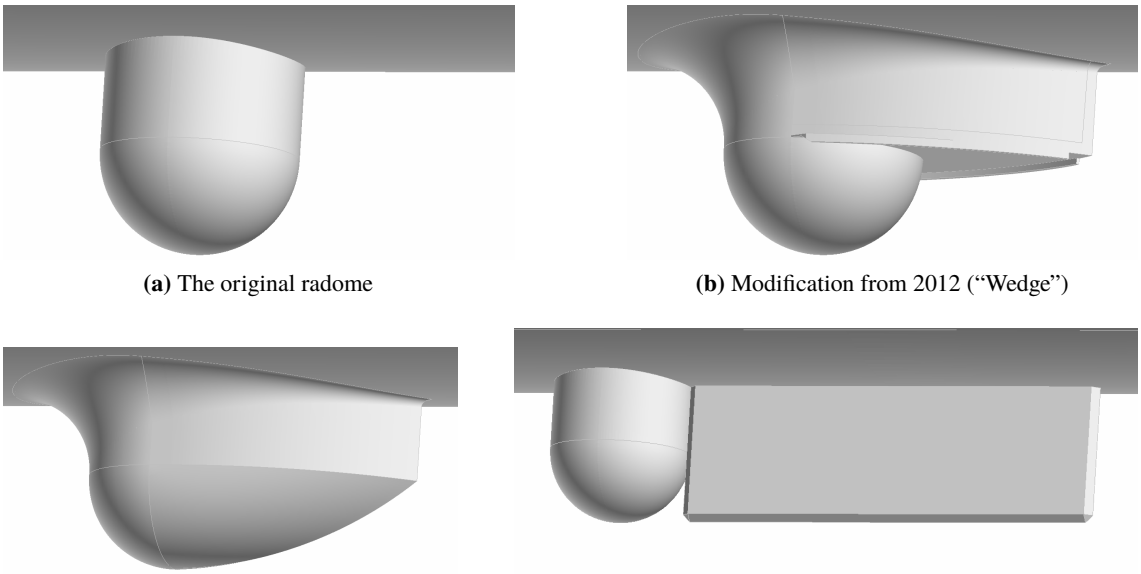

(a) The original radome

(b) Modification from 2012 (“Wedge”)

(c) New radome from 2017 (“Droplet”)

(d) Water tunnel model (“Splitter plate”)

Figure 4.1 *Close-up on the four configurations considered, flow direction from left to right.*

The four configurations considered in this study are shown in Figure 4.1, and described in the following:

“Original radome”: This configuration is simulated again with the new computational domain, to be able to compare forces and oscillation levels with the new geometries. (Figure 4.1a.)

“Wedge”: This is the modification that was built and tested on an aircraft, as well as analyzed computationally, in 2012. It contains a fillet at the front and sides and a convex wedge at the back, in addition to vortex generators at the edges of the wedge. Simulated again for comparison. (Figure 4.1b.)

“Droplet”: This new proposed geometry is designed by NDMA and drawn by AIM Norway. It has the same wedge and fillet as the “Wedge”, but also covers the rear part of the half-sphere. (Figure 4.1c.)

“Splitter plate”: This was one of the configurations used in water tunnel tests reported by L3 Communications in 2010 [10] (“Configuration 17”). Some of the tested configurations were described as designs that “would work from an aerodynamic standpoint”. Both the splitter plate and the other recommended designs extend beyond the geometrical restrictions placed on possible modifications, but this splitter plate is included here for comparison with the “Droplet” design, and to explore the differences between water tunnel tests and CFD analysis. (Figure 4.1d.)

An overview of the cases simulated and reported in this study are given in Table 4.1. Angle of attack and sideslip angle are zero in all the simulations.

Speed (knots)	Original radome	Wedge	Droplet	Splitter plate
280	X	X	X	X
320			X	
360			X	

Table 4.1 *Geometries and flight speeds for the performed simulations.*

5 Calculated quantities

Pressure forces acting on the solid surfaces in the model are recorded as time-series, with forces decomposed in the coordinate directions. Viscous forces are recorded in the same way, but turn out to be negligible compared with the pressure forces.

In addition, the transverse wall shear stress in a point at the fuselage 1.3 m behind the radome centre and the total moment in the vertical direction around the radome centre are recorded. These quantities show the same trend as the pressure forces, and are not presented in this report.

The RMS value of the fluctuations of a given time series $f(t_i)$ is calculated as

$$\widehat{f}_{\mathrm{RMS}} = \sqrt{\frac{1}{N}\sum_{i=1}^{N}\left(f(t_i) - \overline{f}\right)^2},$$

where $\overline{f}$ is the mean of the time series. For any time-series, $f(t_i)$, the power spectral density (PSD) is given by

$$\mathrm{PSD}(k) = \frac{1}{\Delta k}\mathcal{F}_k(f)\,\mathcal{F}_k^*(f),$$

where $\mathcal{F}(f)$ represents the Fourier transform of f.

In addition, shear stress at the surfaces, and pressure, velocity, and vorticity magnitude in the full computational domain are saved at regular intervals for visualization purposes.

6 Simulation results

6.1 RMS of force fluctuations

To illustrate the magnitudes of the oscillating forces for the different recorded quantities, RMS values of the force fluctuations for the original radome at 280 knots are collected in Table 6.1. It is clear that the contributions from the four antennas upstream of the radome and the viscous forces are negligible, compared with the pressure forces on the radome and fuselage. "Fuselage" in this context is the part of the fuselage that is included in the simulation model, as shown in Figure 3.1. (Note that the RMS values of the fluctuations of each part do not add up to the RMS value of the total fluctuations, because the RMS calculation is nonlinear by definition.)

Direction	Pressure, fuselage	Pressure, radome	Pressure, antennas	Pressure, total	Viscous, total
Transverse	440	556	9	982	15
Vertical	406	69	1	415	3
Streamwise	62	171	0	187	4

Table 6.1 *Original radome at 280 knots: RMS values of the force fluctuations (in N) on different surfaces, decomposed into the coordinate directions.*

As the pressure forces in the transverse and vertical directions are dominant, we focus on them in the following. Table 6.2 shows the RMS values of the fluctuations of these forces for the four configurations considered, still at 280 knots.

Force	Orig. radome	"Wedge"	"Droplet"	"Splitter plate"
Total, transverse	1024	312	22	100
Total, vertical	409	87	34	324
Fuselage, transverse	453	174	14	88
Fuselage, vertical	396	107	32	322
Radome, transverse	586	152	2	35
Radome, vertical	67	71	5	15
Fairing, transverse	N/A	183	12	59
Fairing, vertical	N/A	83	3	1

Table 6.2 *RMS values of the pressure force fluctuations (in N) on different surfaces for different configurations, decomposed into the coordinate directions. All data are for flight speed 280 knots.*

Note that "Fairing" in Table 6.2 means everything that is added to the original radome, and "Radome" is the part of the original radome that is unchanged. For the droplet configuration, the "Radome" part has much smaller area than for the original configuration, because the radome is almost completely inside the droplet.

For most of the force components in Table 6.2, the trend is that RMS value of fluctuations are largest for the original radome, followed by the Wedge, the Splitter plate, and smallest for the Droplet. The

exception is the vertical force on the fuselage for the Splitter plate configuration, which is closer to that of the original radome. This would be expected, as the splitter plate does not hinder the vertical separation behind the radome.

6.2 Pressure forces: Time series and power spectral density

We continue to focus on the transverse and vertical components of the total pressure forces acting on the model surface. For each configuration, we present time series and power spectral density (PSD) of the fluctuations (temporal mean value subtracted) of these two pressure force components. If nothing else is stated, the flight speed is 280 knots.

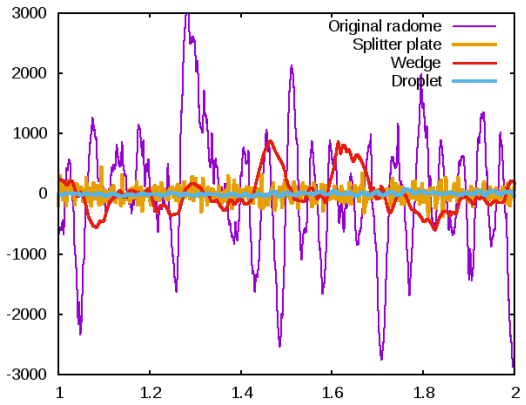

(a) Pressure force (N) as a function of time (s)

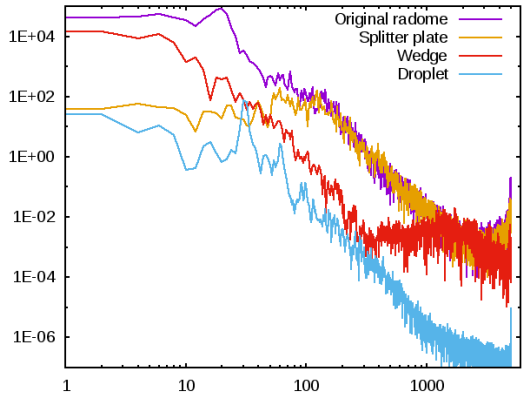

(b) Power spectral density (Pa^2/Hz) as a function of time (s)

Figure 6.1 *All configurations: Fluctuating total transverse pressure force.*

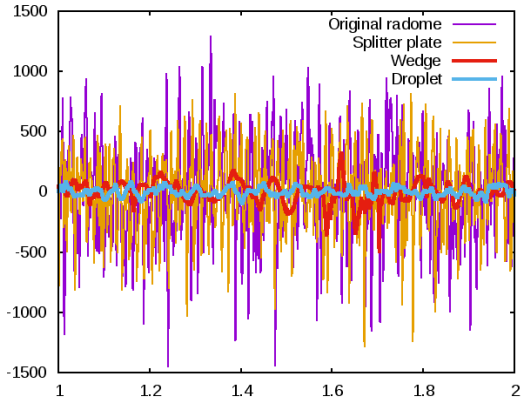

(a) Pressure force (N) as a function of time (s)

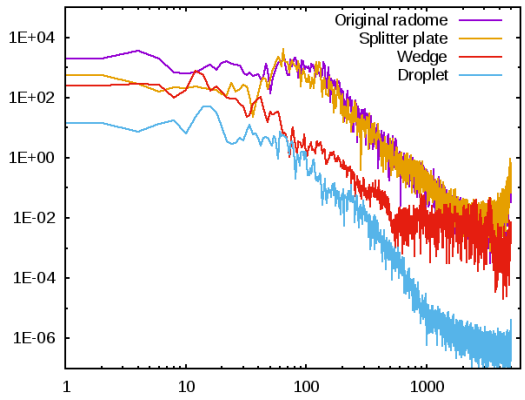

(b) Power spectral density (Pa^2/Hz) as a function of time (s)

Figure 6.2 *All configurations: Fluctuating total vertical pressure force.*

Results for all four configurations are presented in Figures 6.1 and 6.2, for transverse and vertical pressure forces, respectively. To simplify, we use pairwise comparisons in the discussion of the results in the following.

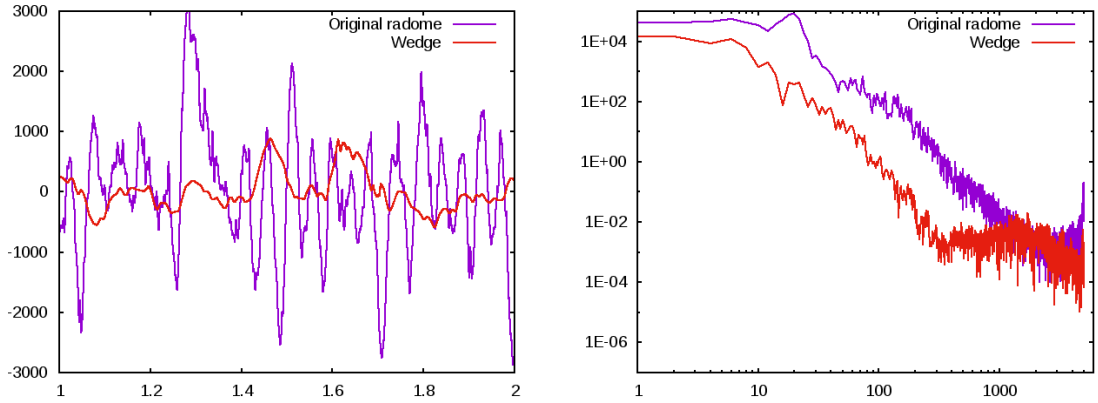

(a) Pressure force (N) as a function of time (s)

(b) Power spectral density (Pa^2/Hz) as a function of time (s)

Figure 6.3 *Original radome vs. Wedge configuration: Fluctuating total transverse pressure force.*

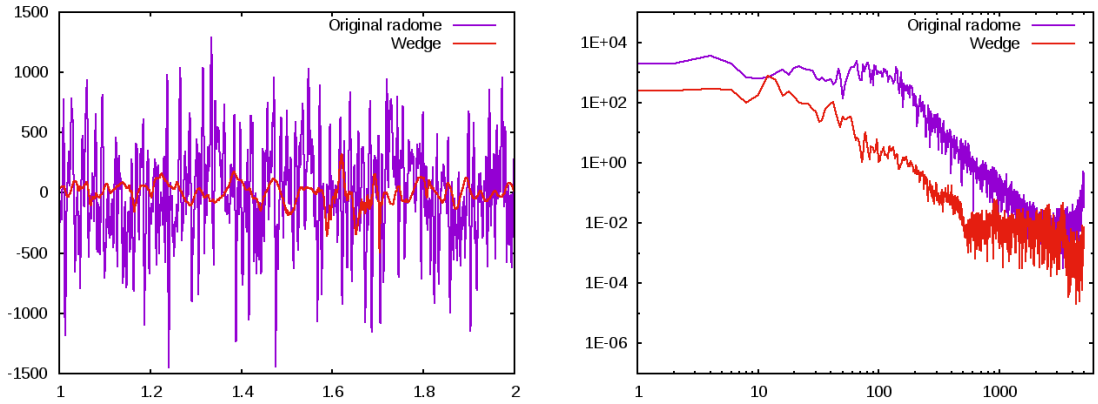

(a) Pressure force (N) as a function of time (s)

(b) Power spectral density (Pa^2/Hz) as a function of time (s)

Figure 6.4 *Original radome vs. Wedge configuration: Fluctuating total vertical pressure force.*

The starting point is the original radome and the Wedge modification from 2012. These are simulated and analyzed again in this new setup, for comparison with the new configurations, and the effect of the Wedge modification is shown in Figures 6.3 and 6.4.

The RMS values in Table 6.2 show that force fluctuations are reduced approximately by a factor of three by the Wedge modification, and the reduction is illustrated in Figures 6.3a and 6.4a. This is in correspondence with the order of magnitude reduction in peak power in acceleration reported in [8], and a similar reduction in PSD of the pressure force fluctuations can be seen in Figures 6.3b and 6.4b.

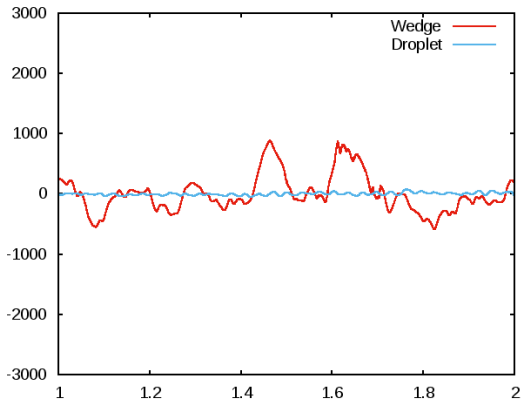

(a) Pressure force (N) as a function of time (s)

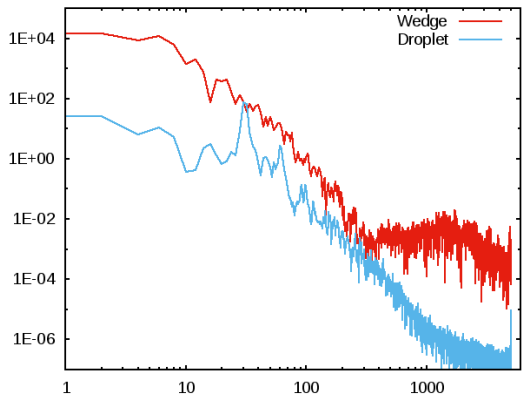

(b) Power spectral density (Pa^2/Hz) as a function of time (s)

Figure 6.5 *Wedge configuration vs. Droplet configuration: Fluctuating total transverse pressure force.*

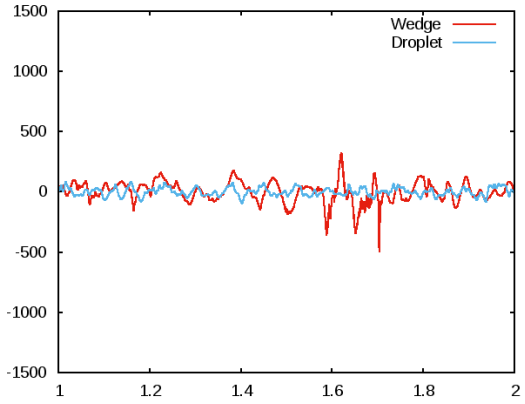

(a) Pressure force (N) as a function of time (s)

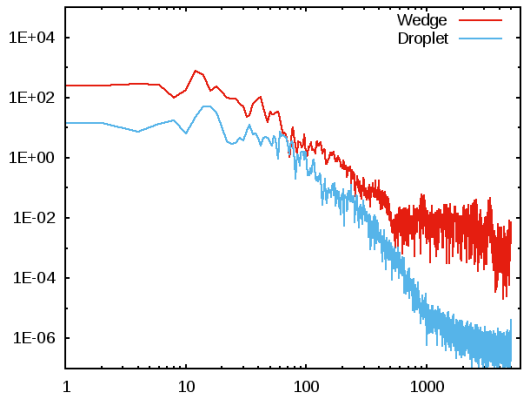

(b) Power spectral density (Pa^2/Hz) as a function of time (s)

Figure 6.6 *Wedge configuration vs. Droplet configuration: Fluctuating total vertical pressure force.*

Table 6.2 shows that force fluctuations are substantially further reduced with the new Droplet configuration, again illustrated by time series in Figures 6.5a (in particular) and 6.6a. Compared with the Wedge configuration, fluctuations are reduced over the full range of frequencies, as seen in Figures 6.5b and 6.6b.

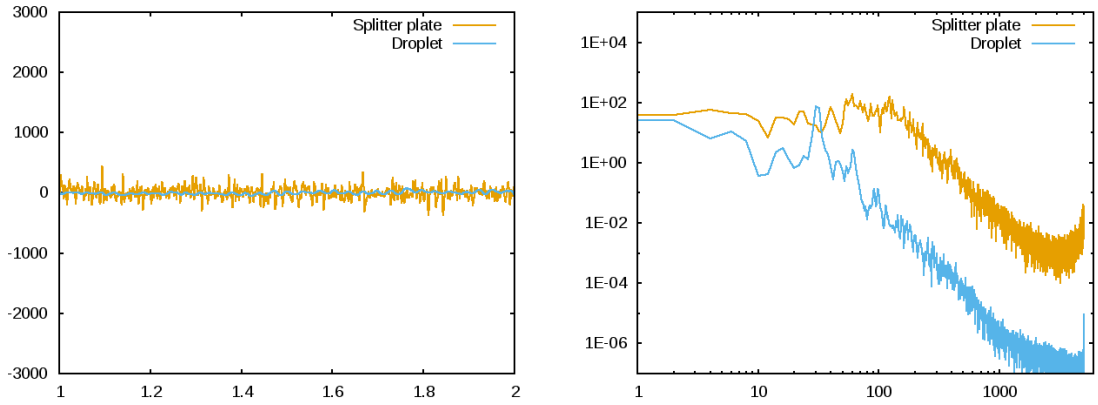

(a) Pressure force (N) as a function of time (s)

(b) Power spectral density (Pa^2/Hz) as a function of time (s)

Figure 6.7 *Splitter plate configuration vs. Droplet configuration: Fluctuating total transverse pressure force.*

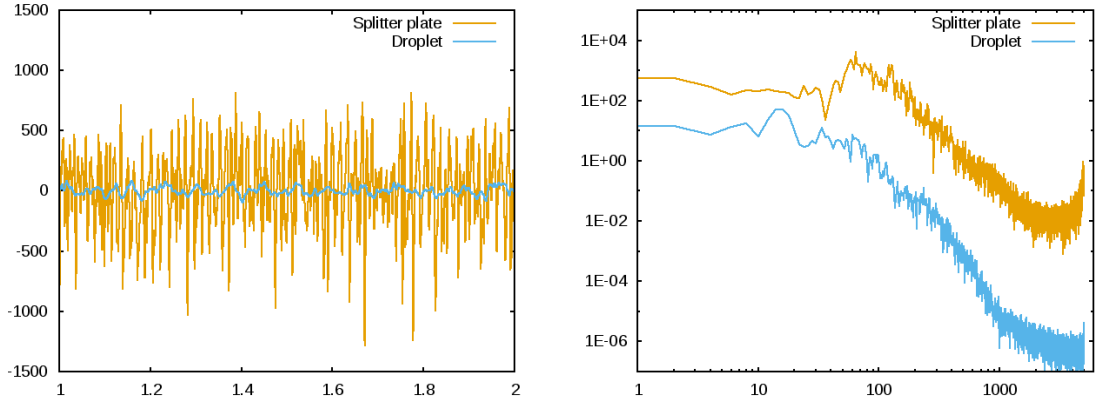

(a) Pressure force (N) as a function of time (s)

(b) Power spectral density (Pa^2/Hz) as a function of time (s)

Figure 6.8 *Splitter plate configuration vs. Droplet configuration: Fluctuating total vertical pressure force.*

The Splitter plate configuration (Figure 4.1d) is compared with the Droplet in Figures 6.7 and 6.8. As seen from these figures, the Splitter plate exhibits considerably more fluctuations than the Droplet.

The Splitter plate is one of the configurations that are predicted in [10] to sufficiently reduce vibrations, but it is clearly not optimal, especially considering that is extends beyond both the geometrical limitations set in 2012 (height and length) and 2017 (length). Low-frequency oscillations, associated with vortex shedding, are reduced, but from around 100 Hz there is little difference from

the original radome, as shown in Figures 6.1b and 6.2b. These frequencies are presumably higher than the main eigenfrequencies of the aircraft structures.

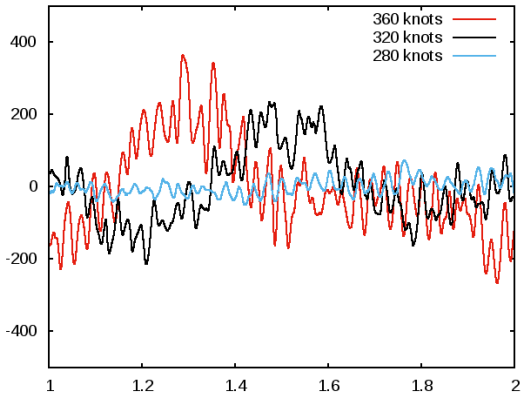

(a) Pressure force (N) as a function of time (s) (Note that the vertical scale is different than in the previous figures)

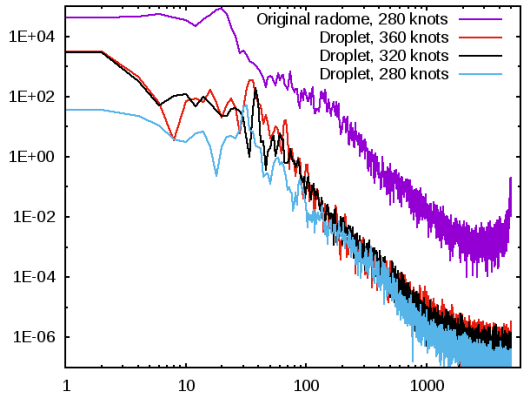

(b) Power spectral density (Pa^2/Hz) as a function of time (s)

Figure 6.9 *Droplet configuration, different speeds: Fluctuating total transverse pressure force.*

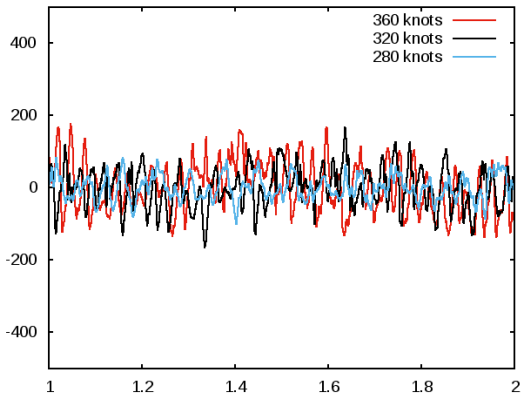

(a) Pressure force (N) as a function of time (s) (Note that the vertical scale is different than in the previous figures)

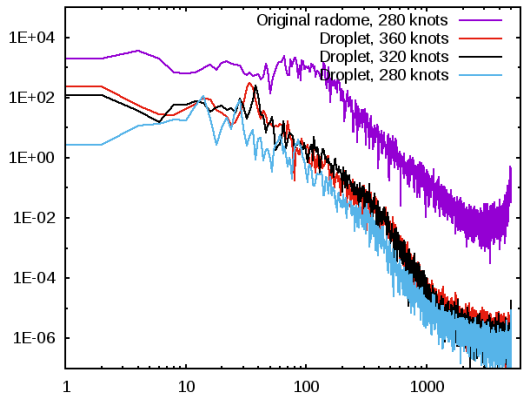

(b) Power spectral density (Pa^2/Hz) as a function of time (s)

Figure 6.10 *Droplet configuration, different speeds: Fluctuating total vertical pressure force.*

We close this section by looking at speed dependency for the Droplet configuration. Figures 6.9 and 6.10 show that the oscillations increase when the speed increases from 280 to 320 knots, and to a smaller extent for further increase to 360 knots. The original radome is included in Figures 6.9b and 6.10b for comparison, and the Droplet fluctuations at the highest speed are still much smaller than for the original radome at 280 knots.

6.3 Flow visualization

There are obviously many features in the three-dimensional, time-dependent flow fields that are not captured in the simple numbers and curves presented in the previous sections. In this section, we present some visualizations of selected quantities to give a better impression of the dominant phenomena in the flow fields.

We present four plots for each of the four configurations. Two different times are selected for each configuration, to give an impression of the time variation of the flow fields. For each time, we present a volume visualization of the vorticity magnitude, which highlights areas containing vortices and strong shear. For the same times we also present friction lines along the surfaces, showing the direction of the local wall shear forces. Even though the shear forces are shown in Section 6.1 to be small compared with the pressure forces, their direction provides an illustration of the flow direction and wake extension close to the surface. If nothing else is stated, the flight speed is 280 knots.

The flow field around the original radome is visualized in Figure 6.11. The interaction between the vortex street and the horseshoe vortex, discussed in Section 2, is illustrated by the sideways movement of the horseshoe vortex. The moving separation points on the radome itself adds to this, and the result is a strongly fluctuating field where the vortex structures itself are highly unsteady over time.

The Wedge configuration was designed to minimize the alternating vortex shedding by filling much of the separation zone behind the radome with a wedge, and to control the separation points as much as possible by introducing additional vortex generations at the wedge edges. This gives a more stable flow field behind the radome, as shown in Figure 6.12. The geometrical restrictions meant that the half-sphere was unmodified, however, leading to some oscillations due to moving separation points at the half-sphere.

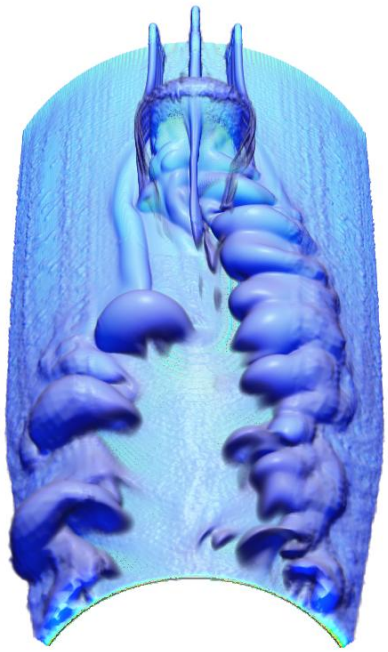

(a) Vorticity magnitude, t=1.730

(b) Vorticity magnitude, t=1.818

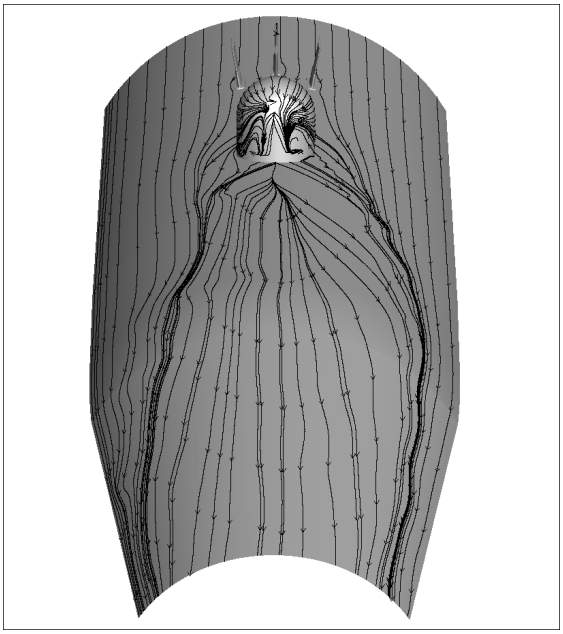

(c) Friction lines, t=1.730

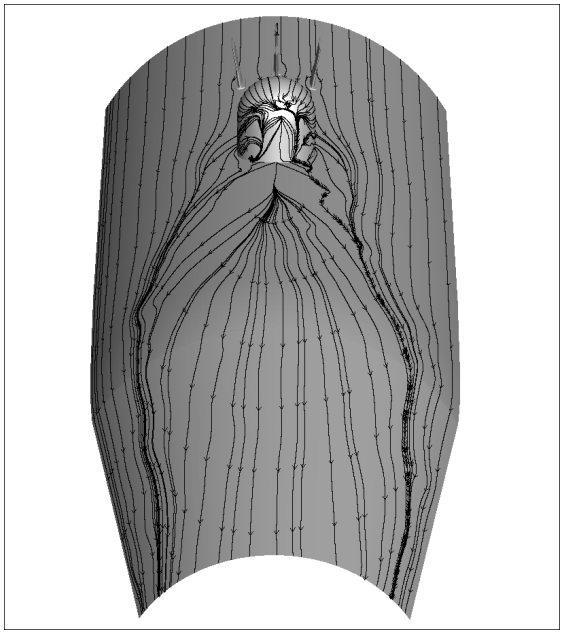

(d) Friction lines, t=1.818

Figure 6.11 *Visualization of the flow around the Original radome configuration.*

(a) Vorticity magnitude, t=1.607

(b) Vorticity magnitude, t=1.682

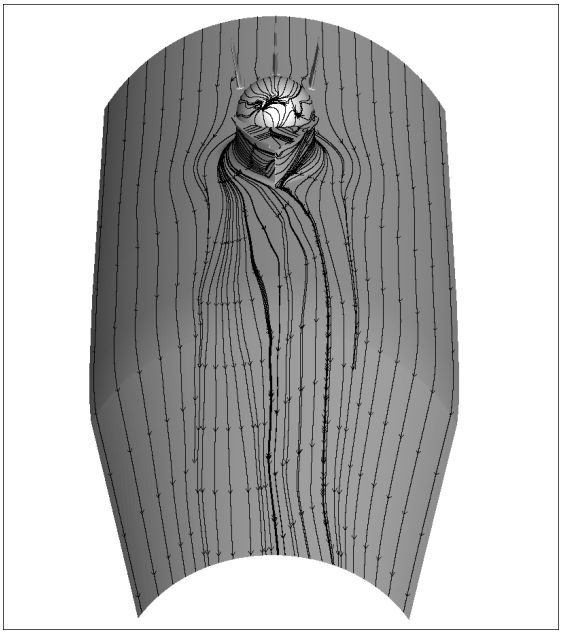

(c) Friction lines, t=1.607

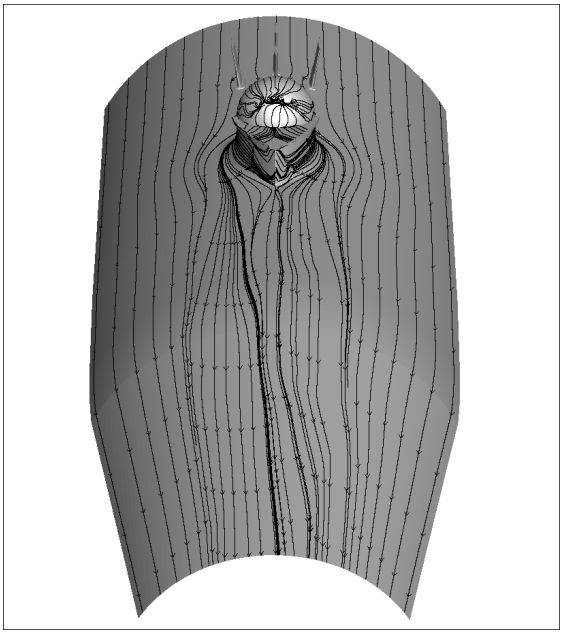

(d) Friction lines, t=1.682

Figure 6.12 *Visualization of the flow around the Wedge configuration.*

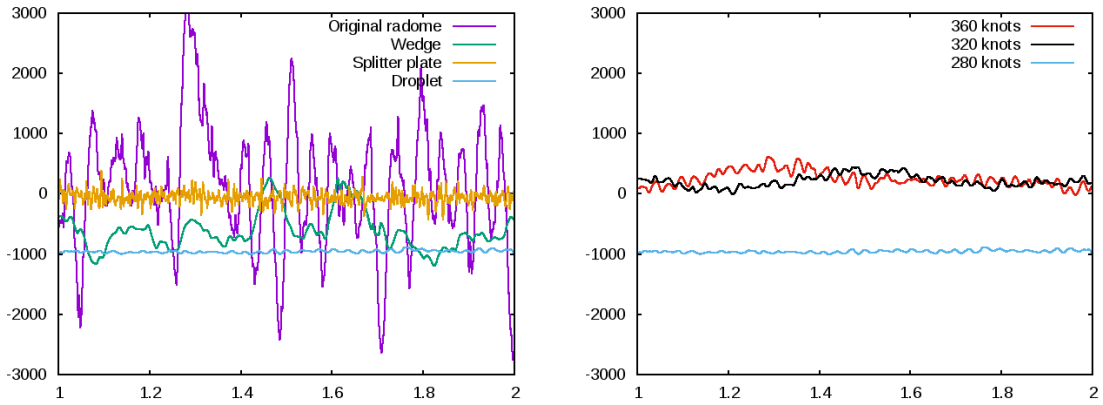

(a) All configurations, 280 knots

(b) Droplet configuration, varying speeds

Figure 6.13 *Total transverse pressure force (N), including the mean values, as a function of time (s).*

To simplify the presentation in Section 6.2, the mean value was subtracted from each of the time series. Figure 6.13 shows the total transverse pressure forces, including the mean values. When the transverse pressure forces do not oscillate around zero, there is an asymmetry in the flow field, and this is most pronounced for the Wedge and Droplet configurations. The explanation is given by the visualization of the Droplet configuration in Figure 6.14. The friction line plots show that a separation occurs on one side of the wedge-tail of the droplet, and the vorticity magnitude plots show how the resulting vortex propagates downstream. In a simulation with perfectly symmetric geometry and numerical mesh, numerical errors smaller than the simulation accuracy will decide which side this separation happens on, whereas in a real flight situations factors like propeller slipstream and sideslip will probably lead to a favoured separation side.

Another possible flow pattern for the Droplet configuration is observed at the higher speeds, where separation occurs at both sides of the droplet tail. The result is a more symmetric flow field, as illustrated by friction lines in Figure 6.15. This explains why the mean values of the pressure force curves in Figure 6.13b are closer to zero for the higher speeds than for 280 knots. It should be noted that small perturbations in the simulations can influence which of these flow patterns that occur in the numerical solution.

With the Droplet configuration, a very stable flow field is obtained behind the radome. In fact, selecting two different times showing different flow patterns proved difficult due to the stability of the flow, as seen in Figure 6.14.

The most important feature of the Droplet is that the separation is reduced and stably located, thus avoiding the alternating vortex shedding from the radome. Combined with the fillet around the radome, which reduces the strength of the horseshoe vortex, this results in an almost stationary flow field behind the radome.

The Splitter plate does not influence the flow directly around the radome, except the middle area behind it, as shown in Figure 6.16. Consequently, the wide horseshoe vortex is similar to the original radome case. The main difference is that the alternating vortex shedding from the radome is suppressed, and consequently the horseshoe vortex is more stable. Figure 6.16 does suggest, however, that the symmetry in the flow pattern may prevent some of the fluctuations from being

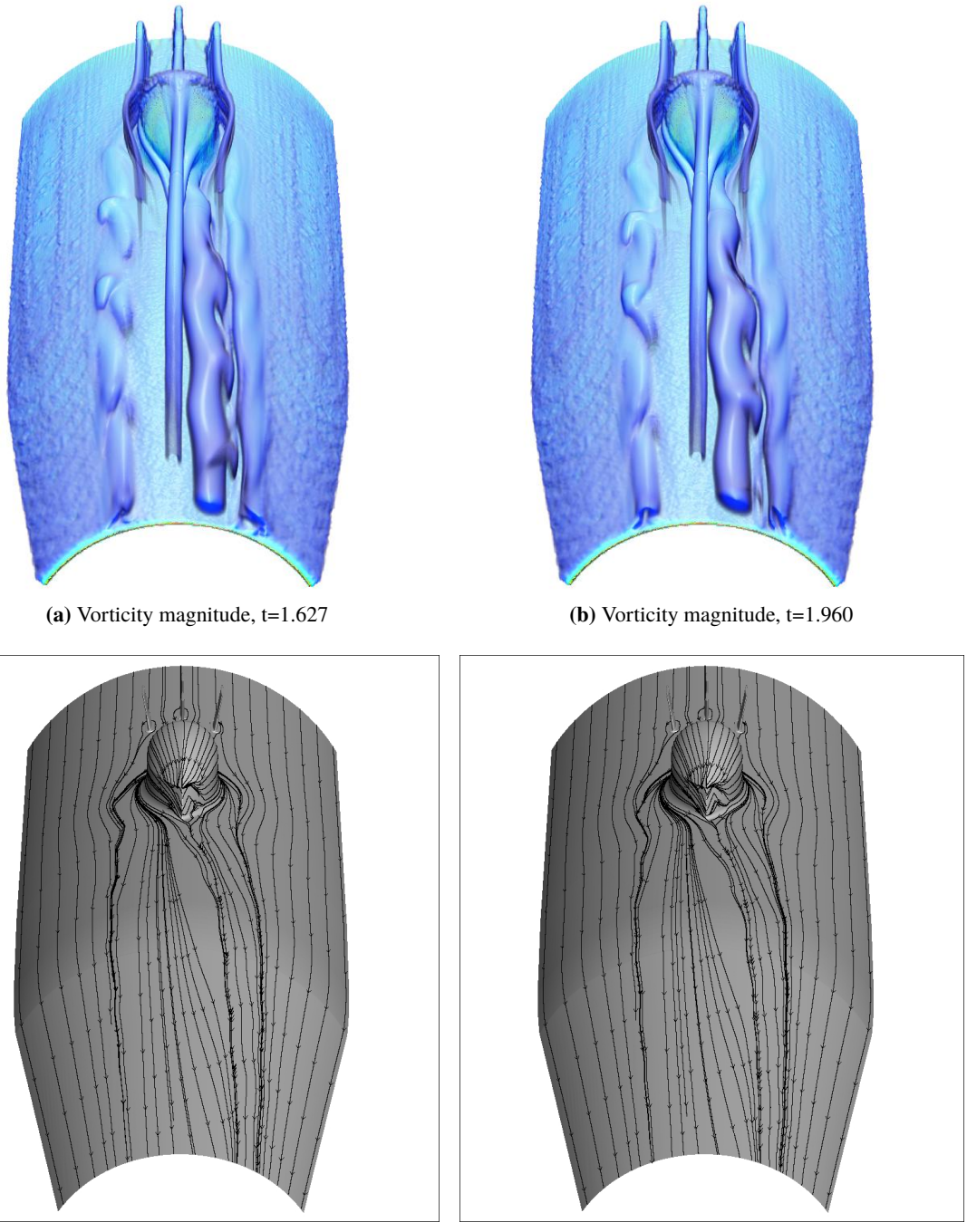

(a) Vorticity magnitude, t=1.627

(b) Vorticity magnitude, t=1.960

(c) Friction lines, t=1.627

(d) Friction lines, t=1.960

Figure 6.14 *Visualization of the flow around the Droplet configuration.*

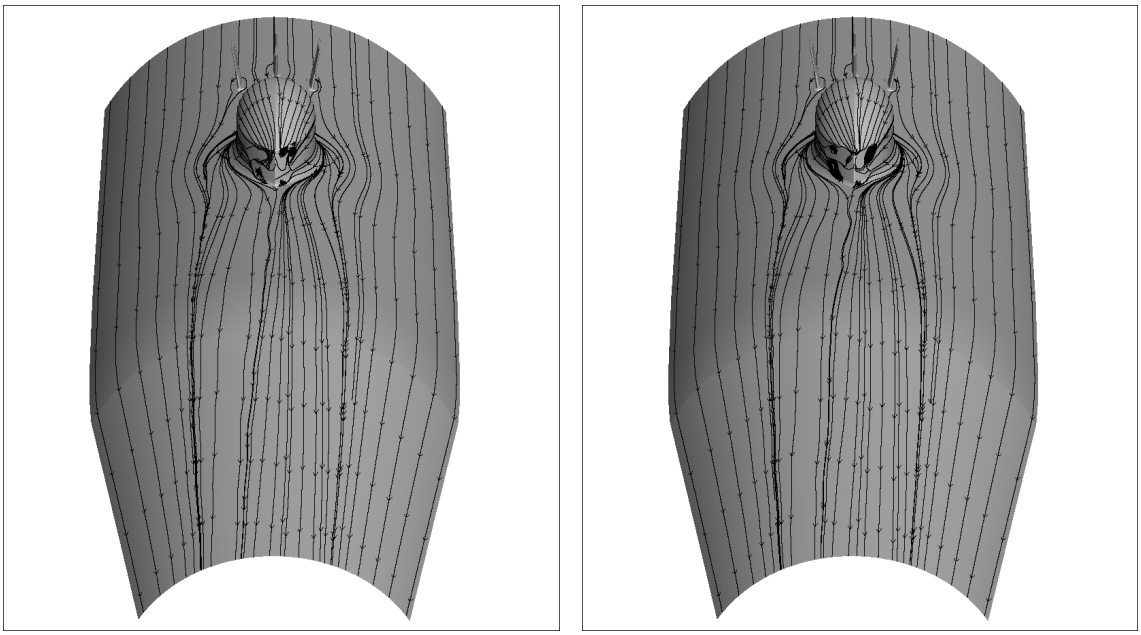

(a) t=1.900 **(b)** t=1.950

Figure 6.15 *Friction lines around the Droplet configuration at 320 knots.*

registered in the pressure force components reported in Section 6.2. That is because transverse pressure forces on opposite sides of the fuselage will cancel each other out in the recorded pressure force shown in Figures 6.1a and 6.7a. In contrast, the vertical pressure force component from this configuration oscillates strongly, as reported in Table 6.2 and shown in Figures 6.2a and 6.8a. This suggests that a simulation with sideslip, which would disturb the symmetry, would record strong oscillations also in in the transverse direction for the Splitter plate configuration.

There are also lots of local fluctuations that may cause vibrations, but probably at frequencies that are higher than the main eigenfrequencies of the aircraft structures.

(a) Vorticity magnitude, t=1.680

(b) Vorticity magnitude, t=1.740

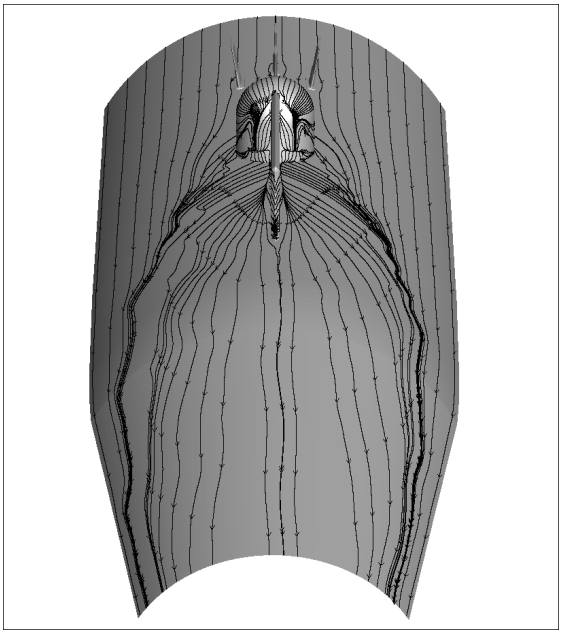

(c) Friction lines, t=1.680

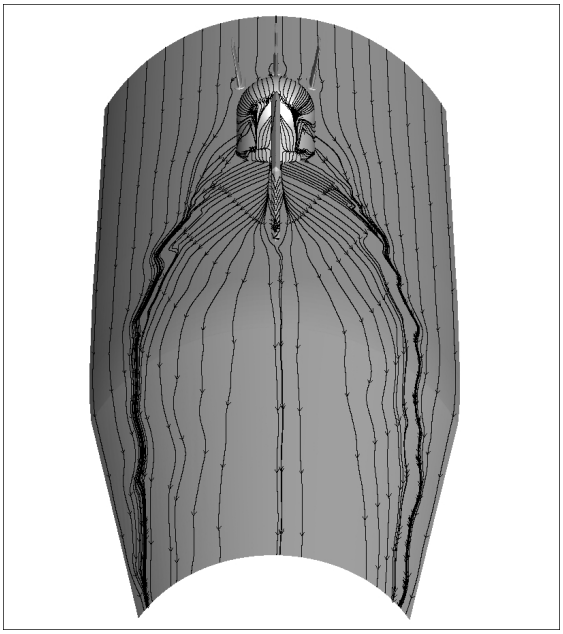

(d) Friction lines, t=1.740

Figure 6.16 *Visualization of the flow around the Splitter plate configuration.*

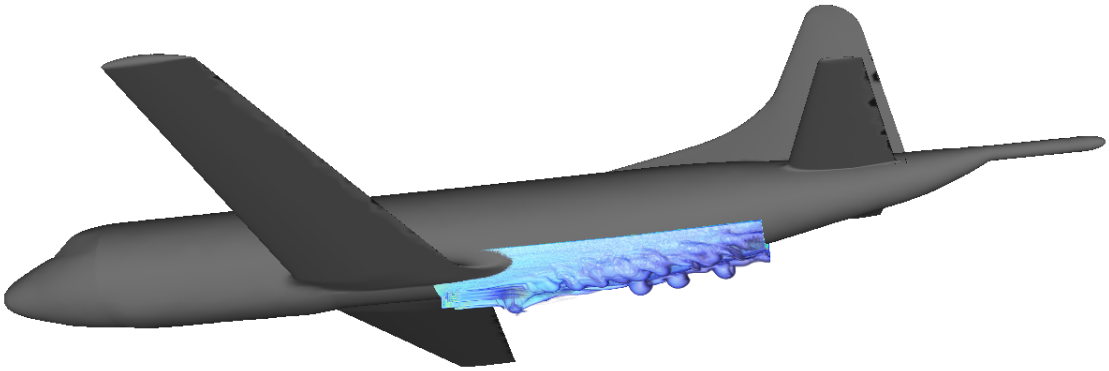

(a) Original radome

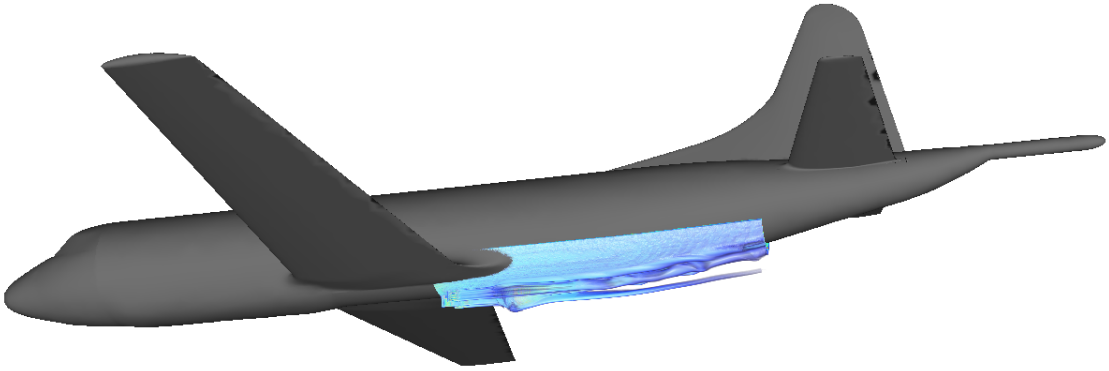

(b) Droplet

Figure 6.17 *Vortex visualization (vorticity magnitude) superimposed on a simplified P-3 model.*

In Figure 6.17, visualizations of the flow field are superimposed on a simplified model of a full aircraft. This illustrates the extension of the computational domain, and the area of direct impact of the flow disturbances behind the radome for the original design and for the new Droplet radome.

7 Conclusions and suggestions for future work

CFD (Computational Fluid Dynamics) analysis of four radome configurations have been performed. The geometries considered are the original radome and three different fairings designed to reduce the fluctuating forces that cause vibrations on the P-3C aircraft.

Time series of pressure force fluctuations on the aircraft are calculated for each of the four configurations. The evaluation of the configurations is based on RMS values and Power Spectral Densities (PSD) from these time series, in addition to investigation of the three-dimensional and time-dependent flow behaviour of the wake of the radome. The latter was achieved by visualization of friction lines and vorticity magnitude, which capture the dominant flow features.

For the "Original radome" configuration, we see from the visualizations that the wake is dominated by interaction between the main horseshoe vortex from the stagnant flow in front of the radome and the vortices created by flow separation behind the radome. This results in rapidly fluctuating forces on the fuselage.

For the "Splitter plate" configuration, the flow field is more symmetric, which imply that the net torque created is small. However, the strength of the vortices is not significantly reduced compared with the original radome configuration. Except for the very low frequency contributions, the Splitter plate and the original radome should generate vibrations of same order of magnitude, which exclude the Splitter plate as a candidate for vibration reduction.

The "Wedge" configuration was designed to minimize the alternating vortex shedding by filling much of the separation zone behind the radome with a wedge, and to control the separation points as much as possible by introducing additional vortex generations at the wedge edges. The Wedge configuration gives a more stable flow field behind the radome, and was demonstrated by previously performed test flights to cause a reduction in energy of the vibrations by around 50%. A restriction on the size of the fairing, however, meant that the half-sphere was unmodified, leading to some oscillations due to moving separation points at the half-sphere.

With less geometrical restrictions, a new design was proposed. With this "Droplet" configuration, a very stable flow field is obtained behind the radome. The most important features of the Droplet are that the separation is reduced and stably located, thus avoiding the unsteady vortex shedding from the radome. Combined with the fillet around the radome, which reduces the strength of the horseshoe vortex, this results in an almost stationary flow field behind the radome.

The result of the analysis is that among the three fairing designs studied to reduce the fluctuating forces causing vibrations in the P-3C aircraft, the Droplet is by far the best. The RMS values of the pressure force fluctuations is a good indication of that. To illustrate, the RMS values in the transverse direction are 1024 N for the original radome, while it is only 22 N for the Droplet. In the vertical direction, the corresponding numbers are 409 N and 34 N – in both cases a reduction by more than an order of magnitude. For comparison, the Wedge configuration resulted in 312 N and 87 N for the corresponding RMS values in the transverse and vertical direction, respectively.

At the present time, a test flight with the Droplet configuration has not been performed. This would be necessary for obtaining precise measures of the vibration reduction for the aircraft. However,

based on results from the flight campaign in 2012, where the effect of the Wedge fairing was measured, we would expect a similar correlation between CFD calculations of fluctuating forces and the measured strength of the vibrations for the new design. We therefore expect that the Droplet, which from simulations imply a significant reduction in fluctuating forces compared with the Wedge, will reduce the vibrations even more.

The analysis presented in this report has shown that with less severe geometry restrictions for the fairing design, reduced aircraft vibrations can be expected. A natural next step would be to try to optimize the new radome shape. The Droplet geometry is based on the Wedge, but is extended to cover all of the back half of the radome half-sphere. One possible variation of this design could be to experiment with concave sides instead of the convex sides of the present droplet. This would direct the flow more straightly backwards, but could also create new separation zones at lower flight speeds. Another design change could be to avoid the sharp trailing edge and instead let the droplet decay smoothly up to the hull. Due to the complexity of the flow field, it is difficult to predict the effect of these changes without performing new simulations.

The ultimate goal in terms of simulations would be to use a model of a full aircraft in order to follow the disturbances caused by the radome all the way to the tail and boom. To reduce the complexity, a natural first step could be to only use the back part of the model, starting some small distance upstream of the radome, thus eliminating the nose, wings and propellers from the simulations. In such a model, simplifications could include modelling the propeller slipstream effects by a general sideslip angle, and introducing local downwards components in the background flow to emulate the wind downwash. The main outcome of such simulations would be a full time-dependent fluctuating pressure field on the back part of the aircraft, which in a next step could provide input for structural analysis.

Bibliography

[1] Ø. Lundberg. Akselerasjonsmålinger på Orion P-3C. FFI-rapport 00/05493, FFI, 2000.

[2] Ø. Lundberg and A. Skaugen. Nye akselerasjonsmålinger på Orion P-3C. FFI-rapport 02/04504, FFI, 2002.

[3] Ø. Lundberg and A. Skaugen. Vibrasjonsmålinger på Orion P-3C 3297 i forbindelse med ny ADF radar. FFI-rapport, Begrenset 04/01935, FFI, 2004.

[4] Ø. Lundberg and A. Skaugen. Vibrasjonsmålinger på Orion P-3C 3298 med modifisert radardome. FFI-rapport, Begrenset 04/04145, FFI, 2004.

[5] B. A. P. Reif and C. E. Wasberg. Numerical simulations of flow-induced vibrations on Orion P-3C. Technical Report FFI/RAPPORT-2003/01331, FFI, 2003.

[6] C. E. Wasberg and B. A. P. Reif. Large-eddy simulation of flow past a wall-mounted cylinder. In B. Skallerud and H. I. Andersson, editors, *MekIT'03 Second national converence on Computational Mechanics*, pages 391–405. Tapir Academic Press, 2003.

[7] B. A. P. Reif and C. E. Wasberg. (U) Numerical simulations of flow-induced vibrations on Orion P-3C – extended study. FFI-rapport, Begrenset FFI/RAPPORT-2004/02740, FFI, 2004.

[8] Ø. Andreassen, C. E. Wasberg, A. Helgeland, M. Tutkun, J. C. Kielland, B. A. P. Reif, Ø. Lundberg, and A. Skaugen. Studies of aerodynamically induced vibrations on the P-3C maritime surveillance aircraft and proposed vibration reducing measures. FFI-rapport 2013/00245, FFI, 2013.

[9] P. Spalart and S. Allmaras. A one-equation turbulence model for aerodynamic flows. *AIAA Paper*, pages 92–0439, 1992.

[10] W. E. Frazier. DF Spin Flow Study Water Tunnel Test Report (Edited for NO). Technical Report G14128.16.20, L3 Communications, 2010.

A Numerical simulation mesh

	Fuselage (centre)	Fuselage (sides)	Radome (incl. front fillet)	Fairing	Fairing (flat plate and vortex gen. – Wedge config.)	Antennas
Max. cell side size	8 mm	16 mm	8 mm	8 mm	4 mm	8 mm
Prism layers	6	6	6	6	N/A	N/A
Tetra growth rate	N/A	N/A	N/A	N/A	1.15	1.5

Table A.1 *Maximum cell side sizes and number of prism layers at different surfaces.*

The mesh used for the simulations is made up by tetrahedral cells, with prism cells used to make the thinnest cells close to the surfaces. The mesh is generated by the meshing program ICEM CFD from Ansys Inc. The global maximum cell side size is 200 mm, and maximum side sizes for the mesh cells at different parts of the geometry are given in Table A.1.

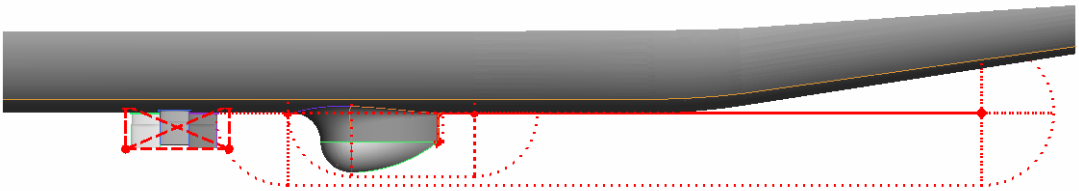

Figure A.1 *Density regions where the maximum mesh cell size is limited.*

Density region	Configurations	Max. cell side size	Number of cells	Radius
Antennas	All	32 mm	N/A	N/A
Inner cylinder	All	16 mm	42	0.672 m
Outer cylinder	All	32 mm	24	0.768 m
Trailing edge	Wedge and Droplet	8 mm	7	0.056 m

Table A.2 *Parameters for the mesh density regions.*

The size of the volume cells are decided by several settings in the meshing program:

- *Prism layers:* For some of the surface parts, a prescribed number of prism layers with a given starting thickness and growth rate are generated. The minimum thickness is 1 mm and the growth rate is 1.5 for each layer, and the number of prism layers for the given surface parts are given in Table A.1.
- *Density regions:* These are regions where the maximum cell size is limited. They are shown in Figure A.1, and their parameters are given in Table A.2. One region contains the antennas upstream the radome, two rounded cylindrical regions cover the radome and modifications, and a small rounded cylindrical region is placed at the trailing edge of the modification (when applicable).
- *Curvature/proximity based refinement:* The grid is refined in areas with large curvature of the geometry or between surfaces close to each other. The default ICEM CFD settings of

2 mm minimum size, 2 elements in a gap, and a maximum refinement of 10 elements around a circle are used.

In terms of the scaled "wall unit" y^+, defined using the friction velocity $u_\star$ and the kinematic viscosity ν as $y^+ = yu_\star/\nu$, the minimum cell thickness of 1 mm in the prism layer corresponds to $y^+ \sim 150$ for 280 knots. To simulate the boundary layer without resorting to the RANS model for turbulence, this cell thickness would have had to be a factor 100 smaller.

All the meshes are smoothed with the default ICEM CFD settings. This involves 5 iterations of smoothing for elements of "Quality" up to 0.2, limited to the worst 1% of elements, and allowing node merging, but not refinement.

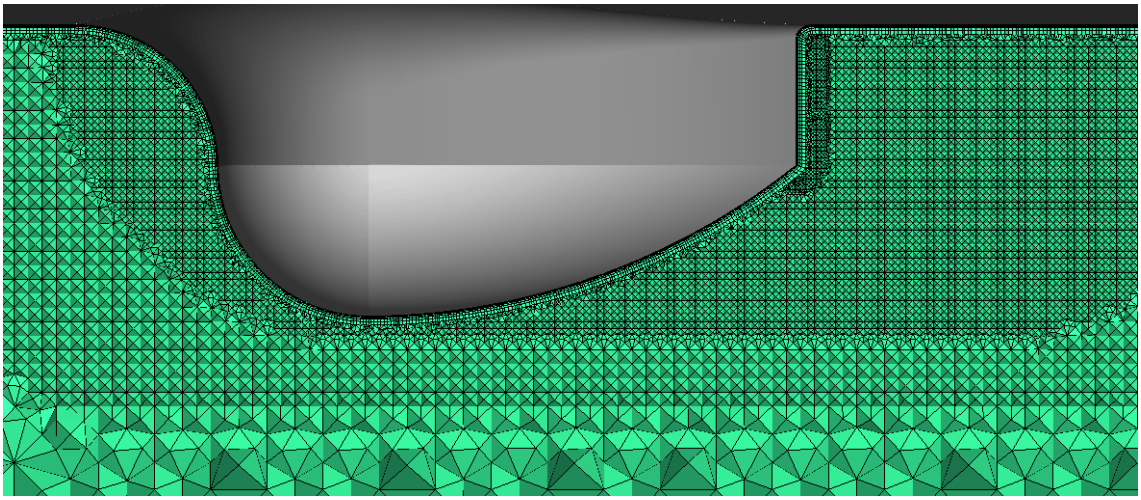

Figure A.2 *Volume mesh in the symmetry plane close to the Droplet.*

A close-up of the mesh in the symmetry plane around the Droplet is shown in Figure A.2. The prism layers are seen as a thin strip close to the surface. Outside the prism layers is the "Inner cylinder" density region, followed by the "Outer cylinder" density region, and the "Trailing edge" density region is seen as a denser area behind the trailing edge. At the bottom of the figure, we see the transition to the largest allowed cells in the simulation. The full mesh in the symmetry plane is shown in Figure A.3.

Configuration	Number of cells
Original radome	25.2 mill.
Wedge	28.1 mill.
Droplet	25.0 mill.
Splitter plate	27.9 mill.

Table A.3 *Number of mesh cells for the different configurations.*

The total number of mesh cells for each configuration is given in Table A.3. Each simulation was run in parallel on 128–256 processors, with typical simulation times of 3–4 days per configuration.

The time-step used in all the simulations is 10^{-4} s, and the Modified Turbulent Viscosity (input parameter for the RANS model) is set to $5.84 \times 10^{-5}\,\mathrm{m}^2/\mathrm{s}$.

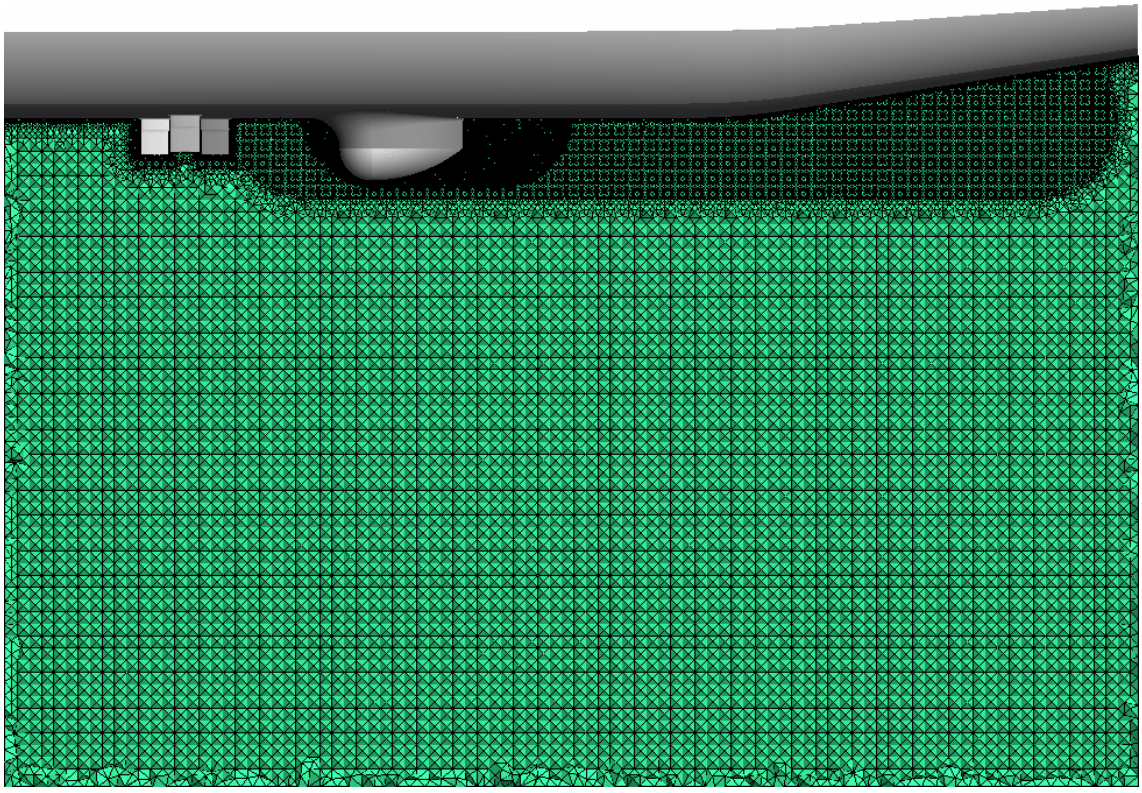

Figure A.3 *Volume mesh in the symmetry plane of the full computational domain for the Droplet configuration.*

About FFI

The Norwegian Defence Research Establishment (FFI) was founded 11th of April 1946. It is organised as an administrative agency subordinate to the Ministry of Defence.

FFI's MISSION

FFI is the prime institution responsible for defence related research in Norway. Its principal mission is to carry out research and development to meet the requirements of the Armed Forces. FFI has the role of chief adviser to the political and military leadership. In particular, the institute shall focus on aspects of the development in science and technology that can influence our security policy or defence planning.

FFI's VISION

FFI turns knowledge and ideas into an efficient defence.

FFI's CHARACTERISTICS

Creative, daring, broad-minded and responsible.

Om FFI

Forsvarets forskningsinstitutt ble etablert 11. april 1946. Instituttet er organisert som et forvaltningsorgan med særskilte fullmakter underlagt Forsvarsdepartementet.

FFIs FORMÅL

Forsvarets forskningsinstitutt er Forsvarets sentrale forskningsinstitusjon og har som formål å drive forskning og utvikling for Forsvarets behov. Videre er FFI rådgiver overfor Forsvarets strategiske ledelse. Spesielt skal instituttet følge opp trekk ved vitenskapelig og militærteknisk utvikling som kan påvirke forutsetningene for sikkerhetspolitikken eller forsvarsplanleggingen.

FFIs VISJON

FFI gjør kunnskap og ideer til et effektivt forsvar.

FFIs VERDIER

Skapende, drivende, vidsynt og ansvarlig.

FFI's organisation

Forsvarets forskningsinstitutt
Postboks 25
2027 Kjeller

Besøksadresse:
Instituttveien 20
2007 Kjeller

Telefon: 63 80 70 00
Telefaks: 63 80 71 15
Epost: ffi@ffi.no

Norwegian Defence Research Establishment (FFI)
P.O. Box 25
NO-2027 Kjeller

Office address:
Instituttveien 20
N-2007 Kjeller

Telephone: +47 63 80 70 00
Telefax: +47 63 80 71 15
Email: ffi@ffi.no

FFI Forsvarets forskningsinstitutt
Norwegian Defence Research Establishment